# Reduced Graphene Oxide Films with Ultrahigh Conductivity as Li-Ion Battery Current Collectors

Yanan Chen,[†] Kun Fu,[†] Shuze Zhu,[‡] Wei Luo,[†] Yanbin Wang,[†] Yiju Li,[†] Emily Hitz,[†] Yonggang Yao,[†] Jiaqi Dai,[†] Jiayu Wan,[†] Valencia A. Danner,[†] Teng Li,[‡] and Liangbing Hu*,[†]

[†]Department of Materials Science and Engineering and [‡]Department of Mechanical Engineering, University of Maryland, College Park, Maryland 20742, United States

S *Supporting Information*
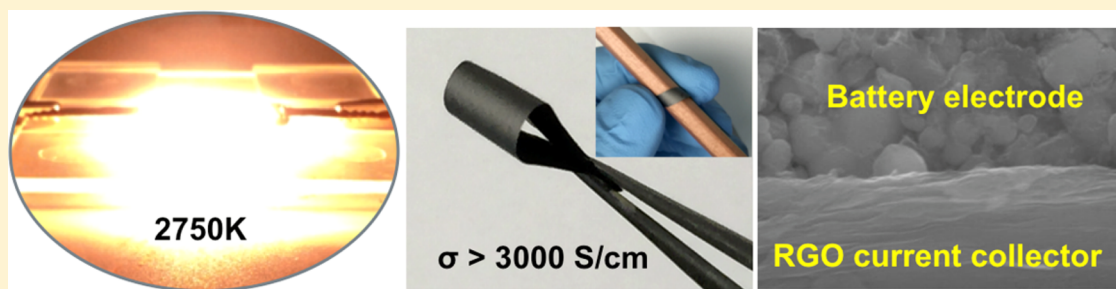
ABSTRACT: Solution processed, highly conductive films are extremely attractive for a range of electronic devices, especially for printed macroelectronics. For example, replacing heavy, metal-based current collectors with thin, light, flexible, and highly conductive films will further improve the energy density of such devices. Films with two-dimensional building blocks, such as graphene or reduced graphene oxide (RGO) nanosheets, are particularly promising due to their low percolation threshold with a high aspect ratio, excellent flexibility, and low cost. However, the electrical conductivity of these films is low, typically less than 1000 S/cm. In this work, we for the first time report a RGO film with an electrical conductivity of up to 3112 S/cm. We achieve high conductivity in RGO films through an electrical current-induced annealing process at high temperature of up to 2750 K in less than 1 min of anneal time. We studied in detail the unique Joule heating process at ultrahigh temperature. Through a combination of experimental and computational studies, we investigated the fundamental mechanism behind the formation of a highly conductive three-dimensional structure composed of well-connected RGO layers. The highly conductive RGO film with high direct current conductivity, low thickness (~4 μm) and low sheet resistance (0.8 Ω/sq.) was used as a lightweight current collector in Li-ion batteries.

KEYWORDS: *High conductivity, high-temperature reduction, reduced graphene oxide, current collector, lightweight, Li-ion batteries*

T he need for lightweight, highly conductive films is ubiquitous in electronics and energy devices. For example, the current collectors used in Li ion batteries, made of copper (Cu) foil at the anode and of aluminum (Al) foil at the cathode, account for 15~50% of the total weight of the device.[1] In aqueous batteries (e.g., NiMH), current collectors account for ~6% of the weight and ~13% of the cost, yet they play a critical role in the electrochemical (EC) performance, particularly the EC stability of the battery and the interface stability of the electrodes. Current collectors used today in aqueous batteries (stainless steel (SS), titanium (Ti), nickel (Ni) foam, Ni-coated SS, and carbon cloth) are heavy, expensive, bulky, and prone to corrosion after prolonged use.[2,3] Competing technologies for battery current collectors have been developed, including carbon nanotube films, graphene films, graphene-coated metals, and flexible graphite foils.[4−9] However, efforts using these forms of nanocarbon have had limited success, especially in terms of conductivity and cost, and do not meet the requirement for practical batteries. Highly conductive carbon nanotube films have been reported for different applications

from transparent electrodes to battery current collectors[10−13] but the application of low-cost carbon nanotubes to batteries remains to be explored. Two-dimensional graphene also shows promise as a low-cost alternative due to the abundance of its raw material, graphite. Freestanding films and composites with exfoliated graphene have been widely reported but the dc conductivity is usually limited to 100 S/cm due to the sheet−sheet junction resistance and small sheet sizes (usually around one micrometer).[14]

Reduced graphene oxide (RGO) nanosheets are extremely attractive due to their large lateral size (up to a few hundred micrometers) after processing, which results in a much lower percolation threshold and fewer junctions in a continuous film, giving rise to high electrical conductivity.[15,16] Various conductive nanostructures based on RGO have been reported
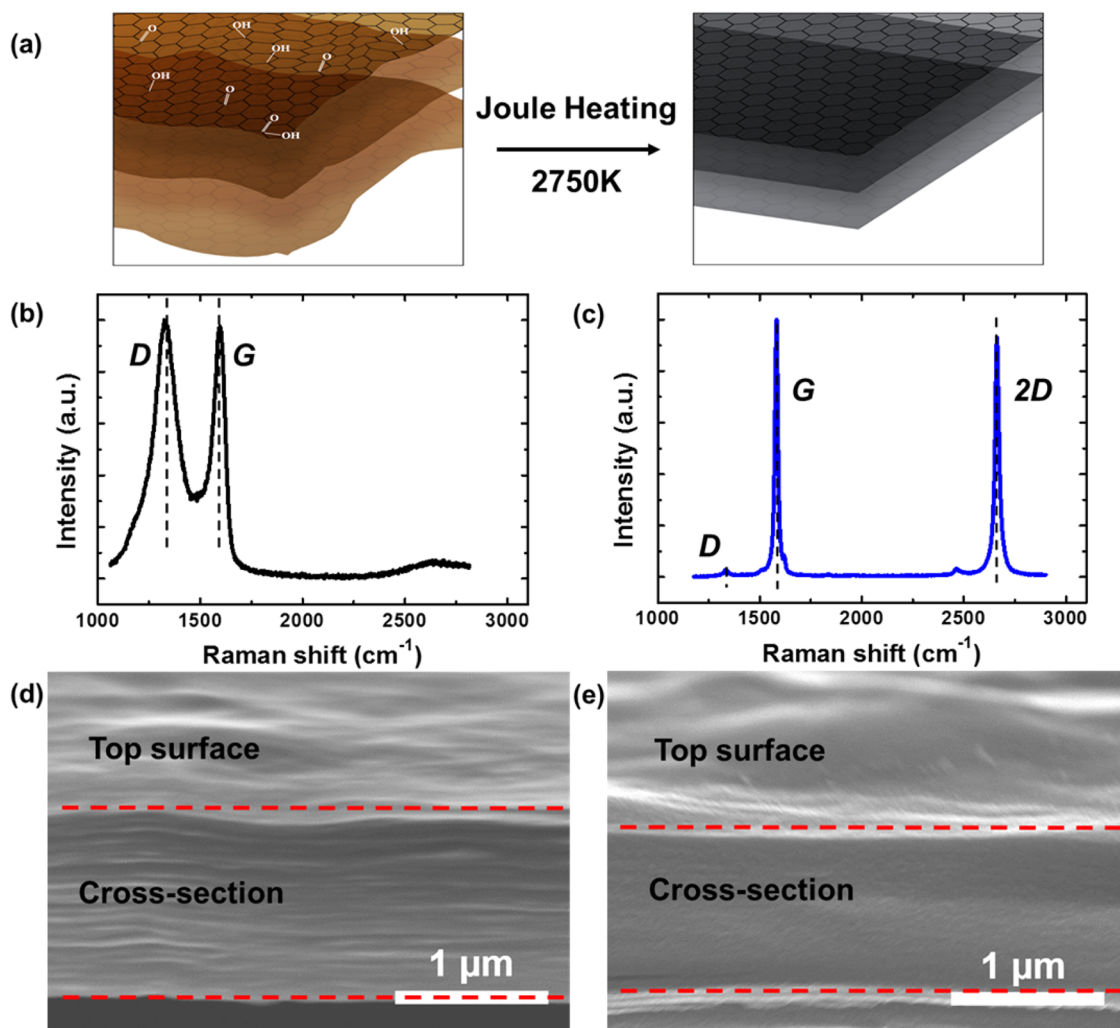
Figure 1. (a) Joule heating at 2750 K for 1 min in vacuum can effectively reduce the RGO, leading to a record-high dc conductivity. (b,c) Raman spectrum comparison of a RGO film annealed in a furnace at 773 K and the same film after the 2750 K annealing for 1 min, respectively. The low D/G ratio and the high 2D peak indicate highly crystalline RGO nanosheets after the process. (d,e) Cross-section SEM images of the RGO film before and after the Joule heating. The Joule heating effectively densifies the RGO films, which significantly increases the coupling in charge transport.

in the past ten years.[17−20] Achieving high-purity, close to pristine graphene through the reduction of graphene oxide (GO) is a major challenge, as the defects and functional groups in partially reduced RGO will largely impede carrier transport. Various reduction methods have been reported, including thermal reduction, chemical reduction and photochemical reduction.[21−27] Effective reduction can dramatically improve the electrical conductivity in RGO nanostructures. However, the highest dc conductivity reported in RGO nanostructure is typically less than 1000 S/cm. The low conductivity of the RGO films prohibits their use as current collectors in Li-ion batteries.

Joule heating is a straightforward method to process and modify carbon nanomaterials, and in particular has been widely explored in carbon nanotubes.[28,29] Selectively burning metallic carbon nanotubes in a carbon nanotube network can effectively increase the on/off current ratio of network-based transistors.[30−32] In this study, we applied Joule heating to effectively reduce GO at an ultrahigh temperature (~2750 K) in a short time (1 min), which led to a record high dc conductivity of 3112 S/cm. The high dc conductivity is related to the highly crystalline graphene structure formed by the high temperature annealing. The electrical current-induced high temperature can

facilitate the thermal reduction of graphene oxides. Different from traditional thermal treatment in a furnace, Joule heating can generate ultrahigh temperature at junction points where the higher electrical resistance is located. The self-healing thermal reduction may have the possibility of forming cross-links between adjacent RGO at defects, which helps to construct highly dense RGO films, leading to high electrical conductivity. The thin (~4 μm thick), freestanding and highly conductive RGO film with a low sheet resistance of 0.8 Ω/sq can be employed to use as ultralight current collectors for lithium-ion batteries.

Starting with graphite, a GO dispersion was prepared by an improved Hummer's method,[33] which was then filtrated to achieve a freestanding GO film with a controlled thickness. Before Joule heating, the GO film was thermally reduced at 773 K in argon (Ar) to preanneal the GO. The preannealed RGO had relatively low conductivity, which was used to trigger the Joule heating by applying electrical current. The temperature of the RGO film increased with applied dc bias, which was monitored through an optical fiber coupled in the homemade setup. During the Joule heating process, a high temperature (2750 K) was detected, which thermally reduced the graphene oxide within minutes, leaving a highly conductive RGO film.
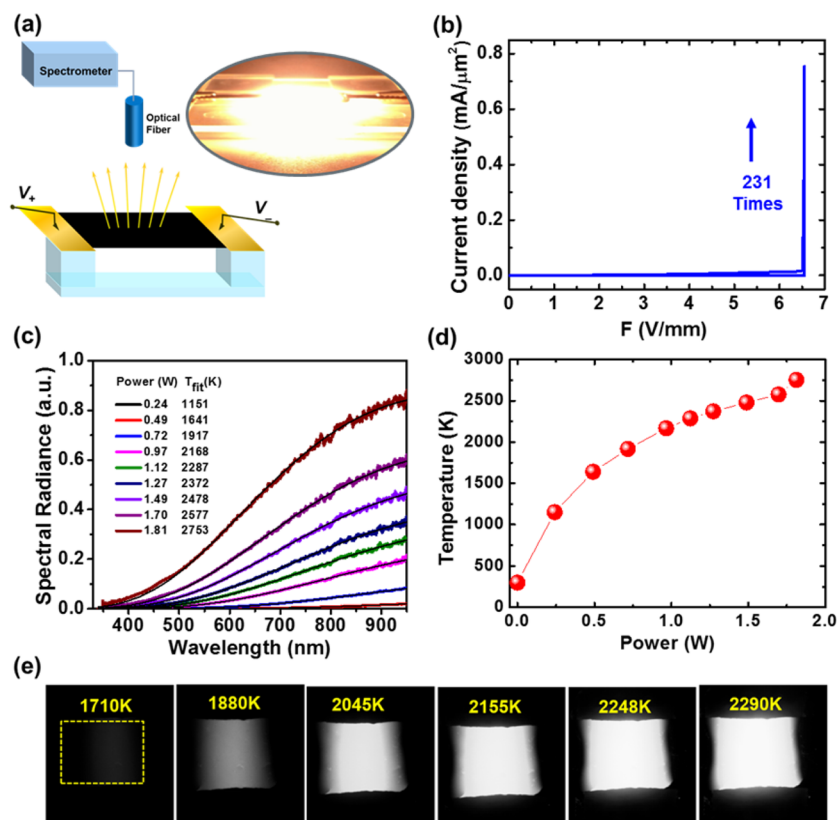
Figure 2. (a) Experiment setup for carrying out the Joule heating experiment in a vacuum chamber with a spectrometer and coupled optical fiber. The bright image is a RGO film under 4 V bias voltage. (b) Current density versus applied electrical field during the Joule heating process for a RGO sample which was preannealed at 773 K for 1 h. Note that the current density increases by 231 times in the sample. (c) Spectral radiance measurement of the same sample with different electrical power inputs. Temperature is determined by fitting the spectra to Planck's law assuming constant emissivity (solid black curves). (d) Fitted temperature of the RGO film versus input electrical power. (e) Sequence of camera images showing the RGO film heating process with increasing applied electrical power. The white part is the illuminated area radiating due to the high temperature induced by electrical current.

Our experimental analysis confirms that most of the defects were removed after the high-temperature process (Figure 1a). Raman spectroscopy was used to study the structural changes of GO before and after Joule heating. Compared to the preannealed GO film (Figure 1b), the D peak of the Joule-heated RGO film associated with the defective carbon (1350 cm^{-1}) is dramatically decreased and the G peak associated with crystalline carbon (1600 cm^{-1}) remains as a high intensity sharp peak (Figure 1c), producing a significant decrease in the ratio of the D mode over G mode (I_D/I_G) from 1.02 to 0.02.

The decreased I_D/I_G ratio indicates that the Joule-heated RGO film can become highly crystallized, with a structural transformation from amorphous carbon to crystallized carbon. In addition, a sharp 2D peak (2690 cm^{-1}) can be observed after Joule heating, with an I_{2D}/I_G ratio of 0.93, confirming the highly crystalline structure of the RGO film after the Joule heating process.[34,35] The characteristic peaks of the Raman spectroscopy show that a highly reduced GO film can be obtained by employing electrical current to generate Joule heating, leading to superior electrical conductivity of the RGO film. The ex situ Raman spectra from the Joule heating process is investigated in detail in the Supporting Information.

Cross-section scanning electron microscopy (SEM) images of the RGO film (Figure 1d,e) reveal a dense structure after the Joule heating compared to pristine. The preannealed GO film shows that stacked RGO layers can be clearly observed with a thickness of 1.25 μm before Joule heating. After electrical current annealing at 2750 K for 1 min in vacuum, the thickness of RGO film decreased to 1.03 μm, exhibiting a relatively dense fracture surface (Figure 1e). The morphology difference may come from the highly stacked RGO flakes that were "melted" or "welded" together during Joule heating at the areas of highest temperature. This densification of RGO flakes is possibly due to the extremely high temperature generated by the current-induced high thermal energy on the junction points of surrounding RGO flakes as well as defects on the surface. The high crystallinity of the RGO nanosheets (increased conduction within each nanosheets) and their dense structure (increased conduction between flakes) simultaneously achieve the record high electrical conductivity of 3112 S/cm.

We investigate the Joule heating process by using the setup shown in Figure 2a. The setup is used to measure the temperature of samples by recording the emitted light during the Joule heating process. In this setup, the preannealed GO film was suspended above a substrate and the two ends of film were bonded by silver paste to connect two copper electrodes. The Joule heating was conducted by applying direct current (dc) through the preannealed GO sample (773 K for 1 h) in a vacuum chamber. The RGO film shines brightly when electrical current is applied. The bright emission, close to white in color, indicates that extreme high temperature is achieved (Figure S1). During the Joule heating, some key parameters including voltage, current, and radiation spectrum were collected to study the thermal behavior of the RGO sample. The spectrometer
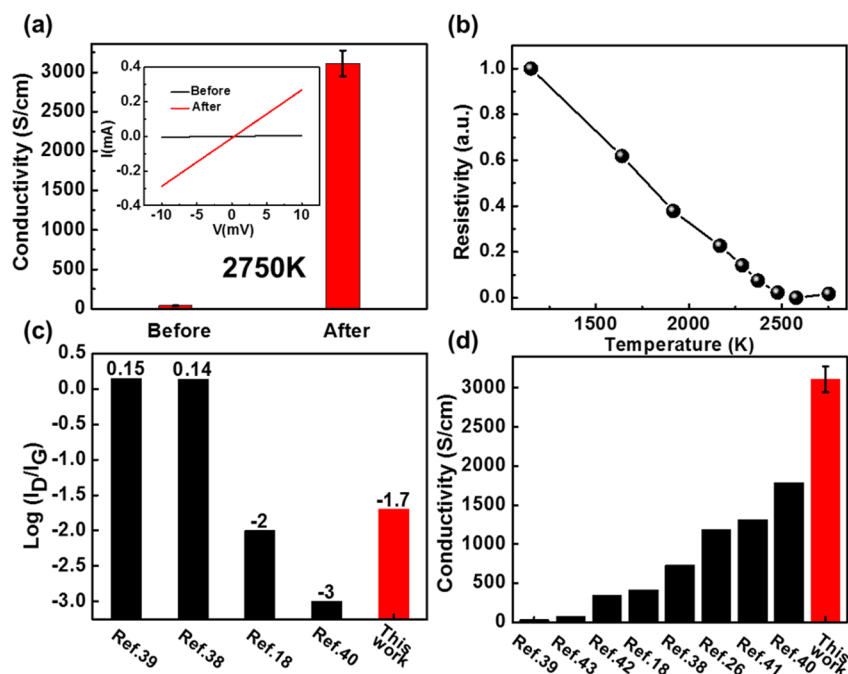
Figure 3. (a) Conductivity of RGO film before and after the 2750 K reduction by the Joule heating. Inset shows the linear scan of the $I-V$ curve. (b) Resistance versus temperature of RGO film during the Joule heating process. (c) Log value of intensity ratio of D peak (1350 cm^{-1}) to G peak (1600 cm^{-1}) (I_D/I_G) of RGO films by different reduction method. (d) The dc conductivity of graphene and RGO nanostructures reported by literatures.

coupled optical fiber having a diameter of 400 μm was placed on top of the RGO sample. The optical fiber and the RGO film have a distance of 15 cm to collect the light emission. Current density was recorded as the applied voltage on the preannealed RGO was increased (Figure 2b). The current density increased slowly with the applied voltage on the RGO film. When the voltage was increased to 6.55 V/mm, the current density instantaneously increased from 0.0033 to 0.76 mA/μm^2, which is around 200 times higher. The significant increase in the conductivity is possibly due to the removal of defects and impurities in RGO film during the high temperature induced by Joule heating.

To characterize the temperature of the RGO films under given voltages, their corresponding emission spectra were recorded by the spectrometer coupled optical fibers, as shown in Figure 2c. The emission spectrum in the wavelength range of 340 to 950 nm was recorded by a spectral measurement system, calibrated by a NIST-traceable light source to ensure accuracy of the measurement. The effect of the glass window of the vacuum chamber has been excluded. The recorded emission spectrum of the RGO film under high temperature was then fitted to the blackbody radiation equation as shown below to extract the in situ temperature of the RGO film

$$I_\lambda(\lambda, T) = \gamma \varepsilon_{gray} \frac{2hc^2}{\lambda^5 \left[\exp\left(\frac{hc}{\lambda k_B T} \right) - 1 \right]}$$

(1)

where k_B is the Boltzmann constant, h is the Planck constant, c is the speed of light, and γ is the scaling constant taking consideration of the unknown coupling factor between the RGO film illumination and the input of the optical fiber. ε_{gray} is a constant emissivity. By a mathematical fitting of each curve from Figure 2c to eq 1, the sample temperature can be extracted.[36,37] Figure 2d shows the results of the fitted temperatures (T) as a function of applied electrical power

(P). Note that 2750 K was the highest temperature obtained by the power supply device in our setup. We envision that a higher temperature can be achieved if a higher power can be applied to the RGO samples. Figure 2e displays a series of images of RGO film taken under different levels of electrical power during the Joule heating process. Each image has an average exposure time of 100 ms. The white part is the illuminated area. The input Joule heating energy is equal to the thermal conduction of the metal contacts on both ends and the blackbody radiation. As the input power increases, the areas exhibiting blackbody radiation become more visible in the images, as appears in the bright areas of Figure 2e, indicating a higher temperature was generated.

The electrical conductivity of RGO before and after high temperature reduction at 2750 K was measured. The slope of the linear scan in Figure 3a shows that the conductivity increases from ~40 to 3023 S/cm with a 76-fold increase. The sample has a size of 2043 μm long, 212 μm wide, and 1.03 μm thick. To obtain accurate values 10 samples were measured and their experimental results were averaged with conductivity value of 3112 $\pm$ 164 S/cm. The resistivity versus the reduction temperature during the Joule heating process was recorded (Figure 3b). The large increase in dc conductivity is due to the improved crystallinity upon the high-temperature treatment, which can be confirmed by the Raman results as well (shown in Figure 1). Note that our I_D/I_G ratio in the Raman spectroscopy after the Joule heating became much lower than reported data in the literature.[18,38−40] Our RGO film reduced at a high temperature with a low I_D/I_G ratio shows a much higher dc conductivity (Figure 3d, Table S1) than RGO films prepared by chemical reduction or thermal reduction.[18,26,38−43] According to literature, Li et al. reported a chemically reduced RGO film with an I_D/I_G ratio of 1.38 and dc conductivity of 33 S/cm,[39] and Mullen et al. reported thermally reduced RGO film with an I_D/I_G ratio of 1.4 S/cm and dc conductivity of 727 S/cm.[38] Recently, Lian et al. reported that a high processing

temperature up to 3123K was used to anneal their heterogeneous microsized fiber with RGOs of two different sizes.[40] Their higher temperature leads to an even lower I_D/I_G ratio of ~0.001 for pure RGOs (Figure 3c). It is interesting that our dc conductivity of 3112 S/cm is much higher than the value 1790 S/cm they achieved for pure RGOs, although their I_D/I_G ratio is lower than ours.

The increased dc conductivity is explained to the possibility that the Joule heating in our process can selectively reduce the high-resistance, defect regions which then self-heal the defect structure. Note the temperature of 2750 K is obtained through fitting the macroscopic blackbody radiation. Local heating with a much higher temperature may possibly generate, although this part of heat cannot be detectable by the radiation spectrum measurement. The local heating at a high temperature in the RGO film, especially in the contact area between RGO nanosheets, could potentially "weld" the RGO nanosheets together through defective carbon atoms to form a 3D cross-linked carbon nanostructure.

The morphology and chemical compositions of RGO films were investigated to understand the record high dc conductivity. Figure 4a,b shows the surface morphology of RGO film before and after the Joule heating, respectively. Magnified morphologies are given in each inset of the SEM images. The RGO film surface becomes much smoother after the 2750 K reduction. Note that the cross-section SEM shown
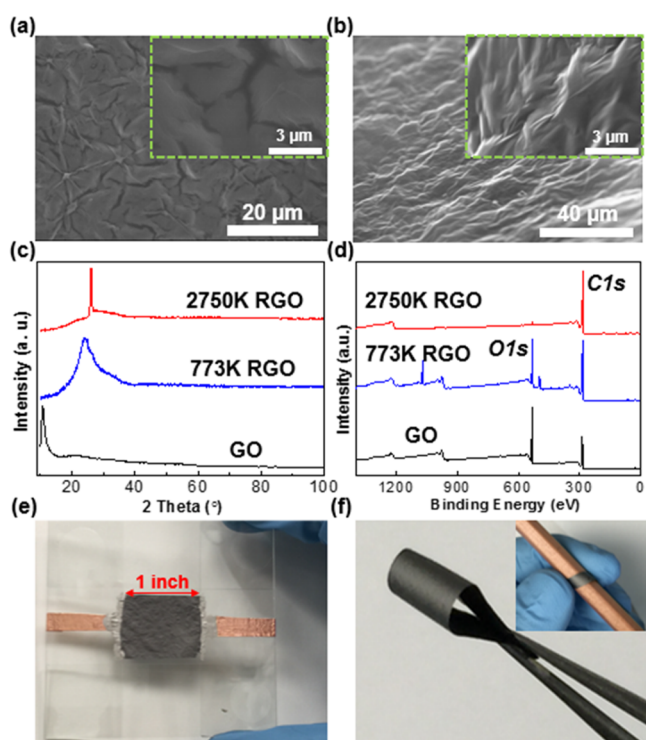

Figure 4. (a) Surface morphology of preannealed GO film. Inset: detail of surface morphology at higher magnification. (b) Surface morphology of the high-temperature reduced RGO film after Joule heating. Inset: detail of surface morphology at higher magnification. (c) XRD patterns of GO, RGO after annealing for 1 h at 773 K (preannealing) and RGO after annealing at 2750 K by Joule heating. (d) XPS scans of the same samples as in (c). (e) A 1 in. × 1 in. RGO sample reduced by the high-temperature process. (f) The high-temperature, Joule-heated RGO is mechanically flexible. Inset: RGO film was bent around a regular pencil.

in Figure 1 reveals that high-temperature reduction can increase the stacking density of the RGO layers. Both the top and cross-section views show the high-temperature process can effectively remove irregularities in the structure. TEM images with an obvious crystalline lattice (Figure S3) reveal the highly crystalline graphene structure of the 2750 K Joule-heated RGO film. The selected-area electron diffraction (SAED) yielding patterns match with those expected for multilayer graphene flakes. Furthermore, the filtered image (Figure S3c) clearly suggests that the 2750 K Joule-heated RGO film shows a high crystallinity with few defects. For the control sample, the 1700 K Joule-heated RGO film shows a poor crystallinity (Figure S4).

X-ray diffraction (XRD) and X-ray photoelectron spectroscopy (XPS) were employed to investigate the microstructure of GO, thermally reduced RGO at 773 K (preannealed), and high-temperature annealed RGO at 2750 K by the Joule heating method. The characteristic peak corresponding to (002) in graphite shows up around ~26.58° after the thermal reduction of GO at 773 K (Figure 4c). After high-temperature reduction by Joule heating, the characteristic peak becomes much more narrow and sharp. On the basis of the peak position, the RGO layer−layer distance was obtained, which decreases from 0.369 nm for 773 K reduction to 0.341 nm for 2750 K reduction. The d-spacing decrease is due to the effective removal of the functional groups in RGO film. Note that the d-spacing is close to the value of graphite (~0.334 nm).[44] The narrow peak at 26.58° indicates that the uniform stacking space in 2750 K RGO is due to the even distribution of current in the RGO film during the Joule heating reduction. XPS scans of the three types of samples were carried out as shown in Figure 4d. The carbon to oxygen atomic ratio is 2.8 in GO, 3.55 in 773 K RGO, and 81.64 in 2750 K RGO, which confirms the effective removal of the functional groups. Note that the 2750 K temperature was only held for 1 min in our experiment to achieve high quality RGO film, which is attractive for fast nanomanufacturing. We demonstrated one RGO film with a size of 1 in. × 1 in. through solution filtration and 1 min high-temperature reduction (Figure 4e). The RGO film is highly flexible, which can be bent down to a small radius with no cracking (Figure 4f).

We attribute the drastic increase in the electrical conductivity of the RGO film after high temperature annealing to the following underlying mechanism: under increasing temperature, the defects in RGO nanolayers (e.g., vacancies, grain boundaries, voids, line defects, and so forth) facilitate the formation of interlayer bridging bonds between neighboring RGO layers, which in turn effectively leads to substantial enhancement of the electrical conductivity of the RGO film. To validate the above-proposed mechanism, we carried out molecular dynamics simulations to model the cross-linking process of neighboring RGO layers (see extended simulation details and results in Supporting Information). For simplicity, we considered a bilayer graphene model with three parallel line defects of width about 0.48 nm in each layer but at different locations (Figure 5a). The bilayer graphene structure is first heated up from 300 to 2500 K in 400 ps, then maintained at 2500 K for 400 ps. During the heating process from 300 to 1420 K, the thermal fluctuation drives the interlayer sliding between the top and bottom graphene layers, suggesting that the interlayer interaction is largely nonbonded type (i.e., van der Waals forces). However, at higher temperatures interlayer bridging bonds start to form when the line defects in two graphene layers come close to each other facilitated by
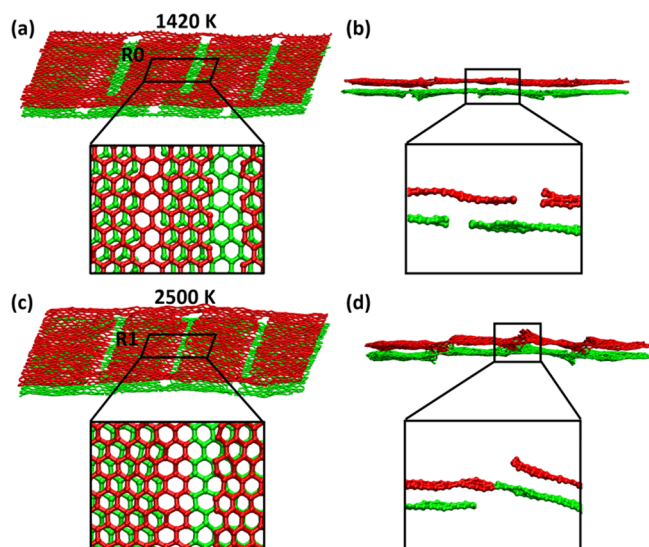
Figure 5. Molecular dynamics simulations demonstrate the defect-facilitated formation of interlayer bridging bonds between two defective neighboring graphene layers at high temperatures. Three parallel line defects exist in each layer (top: red; bottom: green). (a) At 1420 K, the two graphene layers remain separated with no interlayer bridging bond formation. Inset shows the zoomed-in top view of region R0 near the line defects. (b) Side view of (a). Inset shows the zoomed-in cross-section view of region R0. (c) At 2500 K, covalent interlayer bridging bonds form. (d) The side view of (c). Both insets in (c) and (d) clearly show that the left edge of the line defect in the top graphene layer is covalently bonded to the right edge of the neighboring line defect in the bottom graphene layer.

interlayer sliding. Figure 5 plots the snapshot of the bilayer graphene structure at two representative temperatures: at 1420 K (Figure 5a,b), the top and bottom graphene layers remain separated by the equilibrium interlayer distance (0.34 nm) without interlayer bridging bond formation; and at 2500 K, however, covalent interlayer bridging bonds form at the line defects. As clearly shown in Figure 5d, the left edges of all three line defects in the top graphene layer are bonded to the right edges of the neighboring line defects in the bottom graphene layer. The defect-facilitated interlayer bridging bond formation can be attributed to the enhanced reactivity of carbon atoms at the defect edge due to available dangling bonds. High temperatures further increase the reactivity of such carbon atoms with dangling bonds and could also result in migration of defects within the layer, which further facilitates the interlayer bridging bond formation. As a result, the resulting RGO film after high-temperature annealing is expected to be highly cross-linked via rich interlayer bridging bonds, leading to the drastic increase of electrical conductivity. The above modeling results agree with recent work by Barreiro et al. that two overlapped graphene nanosheets can be healed together at high temperature[45] and by Zhang and Li that interlayer bridging bonds can form in a carbon nanoscroll made by rolling up a graphene layer with patterned point defects followed by heating up to a high temperature.[46]

The highly conductive, flexible RGO film with a conductivity of over 3000 S/cm from solution processed GO ink can enable a range of applications from transparent electrodes[16] to current collectors in various batteries. In this work, we demonstrate the highly conductive RGO film as an ultralight current collector
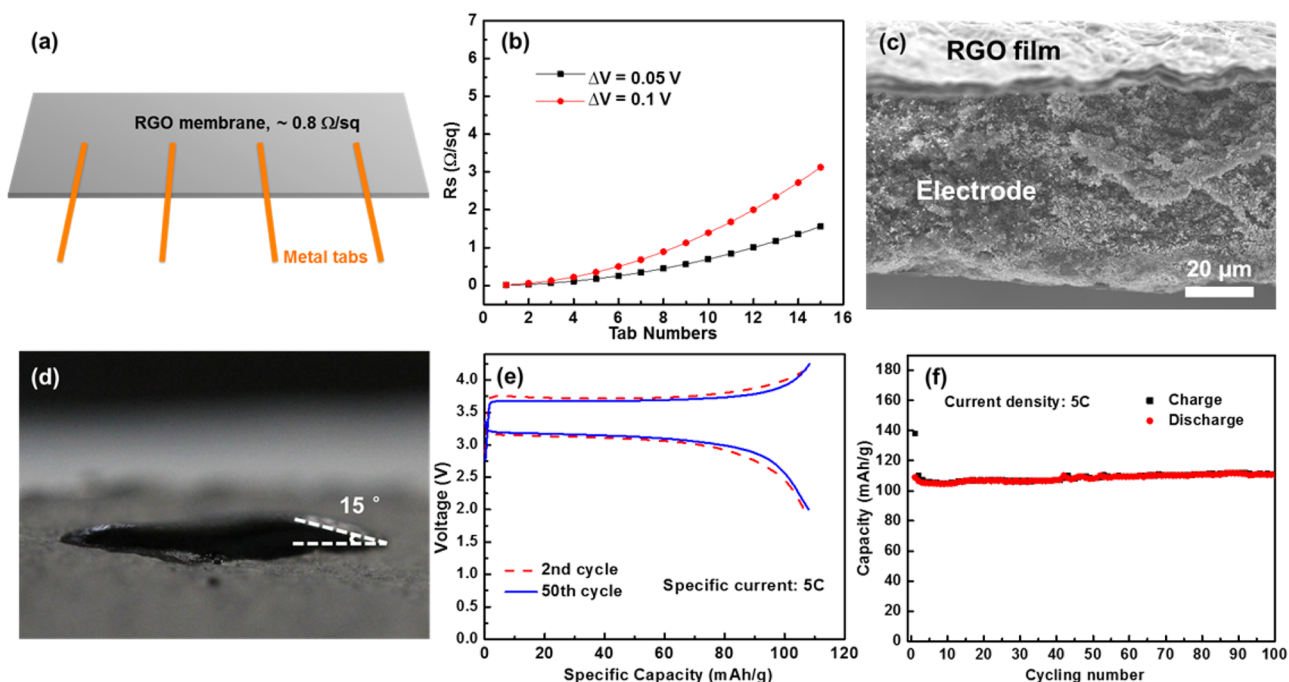
Figure 6. (a) Schematic to show the metal tabs on top of the RGO current collector in an unrolled battery electrode. Note that typical length of a 18 650 cell is 600 mm and width is 50 mm. The metal tabs are designed to conduct the current out. (b) Relationship between sheet resistance and number of tabs in a 18 650 cell with a current density of 2 mA/cm². The values of the overpotential (0.05 and 0.1 V) are due to the resistance of the current collector. Number of tabs decreases as the sheet resistance of the current collector decreases. (c) SEM image of a LiFePO$_4$ composite cathode coated on a RGO current collector, showing excellent contact. (d) Digital image of a LiFePO$_4$ slurry droplet on RGO film with a small contact angle of 15°, illustrating excellent wetting and adhesion properties at the electrode/RGO interface. (e) Galvanostatic discharge/charge profiles of the LiFePO$_4$ electrode with RGO film current collector for the 2nd and 50th cycles. These tests were conducted in the potential range of 2−4.5 V versus Li/Li⁺ at 5C. (f) Cycling performance of the LiFePO$_4$ electrode with RGO film current collector at 5C.

for lithium-ion batteries, where we did initial calculation on the dimensions of the current collectors based on a standard 18 650 cell configuration (see details in Supporting Information). To minimize the IR drop, metal tabs were typically used on the top of the current collectors to conduct global current, which conduct primarily local current (Figure 6a). Here we calculated the dependence of IR drop with the number of tabs and the sheet resistance of the current collector (Figure 6b). For example, when the current density is 2 mA/cm^2, only 11 metal tabs were required with a spacing of 54.5 mm spacing to keep a negligible IR drop of 0.05 V, considering the sheet resistance of RGO film is as low as 0.8 Ω/sq.

The RGO film current collector was demonstrated by constructing a cathode electrode as shown in Figure 6c. A slurry composed of lithium iron phosphate (LiFePO$_4$, LFP), carbon black, and binder (polyvinylidene fluoride, PVdF) with a mass ratio of 7:2:1 was prepared, cast onto the RGO film, and finally dried in a vacuum oven overnight at 373 K to obtain the electrode. The electrode had thickness of ~70 μm and LFP mass loading of 7 mg/cm^2. Figure S7 shows a magnified SEM of the interface between the electrode and the RGO current collector. The dense interface indicates that the dried cathode and RGO formed a good contact in between, which provides good electron transfer pathway between electrode and current collector. The wettability of the RGO film with the fresh slurry ink is shown in Figure 6d. The small contact angle, which is ~15° between the slurry ink and the RGO film, confirms the superior wettability of RGO film. In addition, the rough RGO film surface provides extra surface area for the slurry ink to wet, and such an increase in the surface area can be able to enhance the electrochemical properties of the electrode when high current is applied. The electrochemical performance of the electrode with a RGO film current collector is shown in Figure 6e, which exhibited a smaller polarization in terms of voltage difference between the plateaus of the charge and discharge curves, compared to the electrode that used an Al current collector (Figure S8). A high specific current 5C (1C = 170 mA/g) was applied and the cell with a loading density of 7 mg/cm^2 delivered a capacity of ~110 mAh/g. The cycling performance in Figure 6f exhibits no capacity decay in the measured 100 cycles. Cyclic voltammetry (CV) measurement was used to study the electrochemical stability of the RGO film at high voltage. The result showed good electrochemical stability of RGO film at 4 V (Figure S9). Its good electrochemical performance indicates that the highly conductive, lightweight RGO film can be potentially used as a current collector to replace conventional metal-based current collectors. Meanwhile, the RGO film provides increased surface area to physically contact with electrode so as to improve the interfacial bonding and electrochemical performance. To demonstrate the mechanical stability of RGO film in liquid electrolyte, RGO films were soaked in ethylene carbonate/diethyl carbonate (EC/DEC = 1:1 by volume) solution for 3 days, followed by vacuum drying at 80 °C to measure its mechanical property. Results show that the RGO film still exhibits high flexibility and high tensile strength with a value of 20.1 MPa (Figures S10−S13). In addition, RGO films were wetted by organic solvent N-methyl-2-pyrrolidone (NMP) to mimic the real operation of electrode slurry coating process to check the stability of RGO films in this process. As shown in Figure S14, the RGO film maintained good flexibility and stable structure without swelling after NMP wetting, indicating the compatibility of RGO current collector with commercial slurry coating process.

CONCLUSION

In this work, we report a highly conductive RGO film with record-high dc conductivity up to 3112 S/cm. The highly conductive RGO film is fabricated by a solution based filtration process followed by thermal reduction (773 K) and then a high-temperature reduction (2750 K by Joule heating). The unique high-temperature reduction by Joule heating can effectively remove defects from graphene oxide, improve the crystalline structure of individual RGO nanosheets, and densify their stacking in between, leading to a 231-fold increase in dc conductivity. The drastically increased electrical conductivity of RGO films after high-temperature annealing is attributed to the defect-facilitated cross-linking of neighboring RGO layers, as confirmed by our molecular dynamics simulations. The highly conductive RGO film can have a wide range of applications from microelectronics to large-scale printed electronics. We successfully employed the highly conductive RGO films as current collectors in Li-ion batteries. We envision that the simple but effective Joule heating method can provide a new tool to study and investigate materials under extreme thermal conditions.

ASSOCIATED CONTENT

Ⓢ Supporting Information

The Supporting Information is available free of charge on the ACS Publications website at DOI: 10.1021/acs.nanolett.6b00743.

> Experimental details for material preparation and characterization, Joule heating process and characterization, molecular dynamics simulations, calculation on the dimensions of current collectors, and electrochemical and mechanical evaluations. (PDF)

AUTHOR INFORMATION

Corresponding Author
*E-mail: binghu@umd.edu.

Author Contributions
Y.C. and K.F. contributed equally.

Notes
The authors declare no competing financial interest.

ACKNOWLEDGMENTS

REFERENCES

(1) Johnson, B. A.; White, R. E. *J. Power Sources* **1998**, *70*, 48−54.
(2) Myung, S.-T.; Hitoshi, Y.; Sun, Y.-K. *J. Mater. Chem.* **2011**, *21*, 9891−9911.
(3) Braithwaite, J. W.; Gonzales, A.; Nagasubramanian, G.; Lucero, S. J.; Peebles, D. E.; Ohlhausen, J. A.; Cieslak, W. R. *J. Electrochem. Soc.* **1999**, *146*, 448−456.
(4) Zhou, R.; Meng, C.; Zhu, F.; Li, Q.; Liu, C.; Fan, S.; Jiang, K. *Nanotechnology* **2010**, *21*, 345701.
(5) Park, S.; Shim, H.-W.; Lee, C. W.; Song, H. J.; Park, I. J.; Kim, J.-C.; Hong, K. S.; Kim, D.-W. *Nano Res.* **2015**, *8*, 990−1004.

(6) Yazici, M. S.; Krassowski, D.; Prakash, J. *J. Power Sources* **2005**, *141*, 171−176.

(7) Hu, L.; Wu, H.; La Mantia, F.; Yang, Y.; Cui, Y. *ACS Nano* **2010**, *4*, 5843−5848.

(8) Choi, J. W.; Hu, L.; Cui, L.; McDonough, J. R.; Cui, Y. *J. Power Sources* **2010**, *195*, 8311−8316.

(9) Lytle, J. C.; Wallace, J. M.; Sassin, M. B.; Barrow, A. J.; Long, J. W.; Dysart, J. L.; Renninger, C. H.; Saunders, M. P.; Brandell, N. L.; Rolison, D. R. *Energy Environ. Sci.* **2011**, *4*, 1913−1925.

(10) Hu, L.; Hecht, D. S.; Grüner, G. *Nano Lett.* **2004**, *4*, 2513−2517.

(11) Qu, L.; Vaia, R. A.; Dai, L. *ACS Nano* **2011**, *5*, 994−1002.

(12) Hecht, D. S.; Hu, L.; Irvin, G. *Adv. Mater.* **2011**, *23*, 1482−1513.

(13) Wang, K.; Luo, S.; Wu, Y.; He, X.; Zhao, F.; Wang, J.; Jiang, K.; Fan, S. *Adv. Funct. Mater.* **2013**, *23*, 846−853.

(14) Han, X.; Chen, Y.; Zhu, H.; Preston, C.; Wan, J.; Fang, Z.; Hu, L. *Nanotechnology* **2013**, *24*, 205304.

(15) Lin, X.; Shen, X.; Zheng, Q.; Yousefi, N.; Ye, L.; Mai, Y.-W.; Kim, J.-K. *ACS Nano* **2012**, *6*, 10708−10719.

(16) Zhao, J.; Pei, S.; Ren, W.; Gao, L.; Cheng, H.-M. *ACS Nano* **2010**, *4*, 5245−5252.

(17) Xu, Z.; Zhang, Y.; Li, P.; Gao, C. *ACS Nano* **2012**, *6*, 7103−7113.

(18) Cruz-Silva, R.; Morelos-Gomez, A.; Kim, H.; Jang, H.; Tristan, F.; Vega-Diaz, S.; Rajukumar, L. P.; Elías, A. L.; Perea-Lopez, N.; Suhr, J.; Endo, M.; Terrones, M. *ACS Nano* **2014**, *8*, 5959−5967.

(19) Jang, H. D.; Kim, S. K.; Chang, H.; Choi, J.-H.; Cho, B.-G.; Jo, E. H.; Choi, J.-W.; Huang, J. *Carbon* **2015**, *93*, 869−877.

(20) Han, T. H.; Huang, Y.-K.; Tan, A. T. L.; Dravid, V. P.; Huang, J. *J. Am. Chem. Soc.* **2011**, *133*, 15264−15267.

(21) Wu, Z. S. *ACS Nano* **2009**, *3*, 411−417.

(22) Pei, S. *Carbon* **2010**, *48*, 4466−4474.

(23) Moon, I. K.; Lee, J.; Ruoff, R. S.; Lee, H. *Nat. Commun.* **2010**, *1*, 73.

(24) Williams, G.; Seger, B.; Kamat, P. V. *ACS Nano* **2008**, *2*, 1487−1491.

(25) Cote, L. J.; Cruz-Silva, R.; Huang, J. *J. Am. Chem. Soc.* **2009**, *131*, 11027−11032.

(26) Pei, S.; Cheng, H.-M. *Carbon* **2012**, *50*, 3210−3228.

(27) Bagri, A.; Mattevi, C.; Acik, M.; Chabal, Y. J.; Chhowalla, M.; Shenoy, V. B. *Nat. Chem.* **2010**, *2*, 581−587.

(28) Mann, D.; Kato, Y. K.; Kinkhabwala, A.; Pop, E.; Cao, J.; Wang, X.; Zhang, L.; Wang, Q.; Guo, J.; Dai, H. *Nat. Nanotechnol.* **2007**, *2*, 33−38.

(29) Liu, P.; Sun, Q.; Zhu, F.; Liu, K.; Jiang, K.; Liu, L.; Li, Q.; Fan, S. *Nano Lett.* **2008**, *8*, 647−651.

(30) Cao, Q.; Rogers, J. A. *Adv. Mater.* **2009**, *21*, 29−53.

(31) Ishikawa, F. N.; Curreli, M.; Olson, C. A.; Liao, H.-I.; Sun, R.; Roberts, R. W.; Cote, R. J.; Thompson, M. E.; Zhou, C. *ACS Nano* **2010**, *4*, 6914−6922.

(32) Wang, C.; Zhang, J.; Ryu, K.; Badmaev, A.; De Arco, L. G.; Zhou, C. *Nano Lett.* **2009**, *9*, 4285−4291.

(33) Marcano, D. C.; Kosynkin, D. V.; Berlin, J. M.; Sinitskii, A.; Sun, Z.; Slesarev, A.; Alemany, L. B.; Lu, W.; Tour, J. M. *ACS Nano* **2010**, *4*, 4806−4814.

(34) Ferrari, A. C.; Basko, D. M. *Nat. Nanotechnol.* **2013**, *8*, 235−246.

(35) Dresselhaus, M. S.; Jorio, A.; Hofmann, M.; Dresselhaus, G.; Saito, R. *Nano Lett.* **2010**, *10*, 751−758.

(36) Kim, Y. D.; Kim, H.; Cho, Y.; Ryoo, J. H.; Park, C.-H.; Kim, P.; Kim, Y. S.; Lee, S.; Li, Y.; Park, S.-N.; Shim Yoo, Y.; Yoon, D.; Dorgan, V. E.; Pop, E.; Heinz, T. F.; Hone, J.; Chun, S.-H.; Cheong, H.; Lee, S. W.; Bae, M.-H.; Park, Y. D. *Nat. Nanotechnol.* **2015**, *10*, 676−681.

(37) Freitag, M.; Chiu, H.-Y.; Steiner, M.; Perebeinos, V.; Avouris, P. *Nat. Nanotechnol.* **2010**, *5*, 497−501.

(38) Wang, X.; Zhi, L.; Müllen, K. *Nano Lett.* **2008**, *8*, 323−327.

(39) Yang, X.; Cheng, C.; Wang, Y.; Qiu, L.; Li, D. *Science* **2013**, *341*, 534−537.

(40) Xin, G.; Yao, T.; Sun, H.; Scott, S. M.; Shao, D.; Wang, G.; Lian, J. *Science* **2015**, *349*, 1083−1087.

(41) Su, Q.; Pang, S.; Alijani, V.; Li, C.; Feng, X.; Müllen, K. *Adv. Mater.* **2009**, *21*, 3191−3195.

(42) Chen, H.; Müller, M. B.; Gilmore, K. J.; Wallace, G. G.; Li, D. *Adv. Mater.* **2008**, *20*, 3557−3561.

(43) Li, D.; Müller, M. B.; Gilje, S.; Kaner, R. B.; Wallace, G. G. *Nat. Nanotechnol.* **2008**, *3*, 101−105.

(44) Pierson, H. O. *Handbook of Carbon, Graphite, Diamonds and Fullerenes: Processing, Properties and Applications*; William Andrew: New York, 2012.

(45) Barreiro, A.; Börrnert, F.; Rümmeli, M. H.; Büchner, B.; Vandersypen, L. M. K. *Nano Lett.* **2012**, *12*, 1873−1878.

(46) Zhang, Z.; Li, T. *Nanoscale Res. Lett.* **2011**, *6*, 470.

Supporting Information

Reduced Graphene Oxide Films with Ultra-High Conductivity as Li-ion Battery Current Collectors

Yanan Chen[1,a], Kun Fu[1,a], Shuze Zhu[2], Wei Luo[1], Yanbin Wang[1], Yiju Li[1], Emily Hitz[1], Yonggang Yao[1], Jiaqi Dai[1], Jiayu Wan[1], Valencia A. Danner[1], Teng Li[2], Liangbing Hu[1,*]

[1]Department of Materials Science and Engineering, University of Maryland College Park, College Park, Maryland, 20742

[2]Department of Mechanical Engineering, University of Maryland College Park, College Park, Maryland, 20742

* Corresponding author Email: binghu@umd.edu

(a) Equally contributed.

Material preparation and characterization

Preparation of graphene oxide (GO): The GO ink was prepared according to the improved Hummer's method.[1] In brief, 1.5 g natural graphite flakes and 9 g $KMnO_4$ were added into 200 mL mixed acid of H_2SO_4/H_3PO_4 (volume ratio 9:1), and then the suspended solution was heated and stirred under 50 $^{\circ}$C for 12 hours. Subsequently, 200 mL ice mixed with 3 mL H_2O_2 was poured into above mixture solution after it was cooled down to room temperature. Next, The GO was washed with 5% HCl solution and DI water by centrifugation for several times. Finally, the GO was diluted with DI water to obtain a 2.5 mg mL^{-1} GO solution.

Characterization methods: XRD pattern was collected by the D8 Advanced (Bruker AXS, WI, USA). Raman spectroscopy was obtained by a commercial micro Raman spectrometer (Labram Aramis model manufactured by Horiba Jobin Yvon) using a 633 nm He-Ne laser. The morphology of the RGO samples was examined by a Hitachi SU-70 field emission scanning electron microscopy (SEM), and a JEOL JEM 2100 transmission electron microscope (TEM) at an accelerating voltage of 200 kV. XPS data were collected on a Kratos Axis 165 x-ray photoelectron spectrometer.

Battery performance evaluation: Cells were tested using a LAND-CT 2001A battery test system. The galvanostatic charge-discharge tests were conducted in a voltage range of 4.5 V to 2 V versus Li/Li$^+$. Lithium was used as the counter and reference electrode. The liquid electrolyte was 1 M LiPF$_6$ in an ethylene carbonate/diethyl carbonate (EC: DEC = 1:1 by volume) mixture solution. All the cells were assembled in a high-purity argon-filled glovebox.

The uniaxial tensile test was conducted using a dynamic mechanical analyzer (Q800 DMA, TA Instruments). The samples were mounted using thin film tension clamps with a compliance of about 0.3μm N^{-1}. The tests were carried out by controlling the strain ramp rate of 0.2% min^{-1} until fracture with a preload of 0.01 N. The RGO samples used for the tensile test were 15mm long, 5mm wide and 4μm thick. The Al foil used for the tensile test was 15mm long, 5mm wide and 16μm thick.
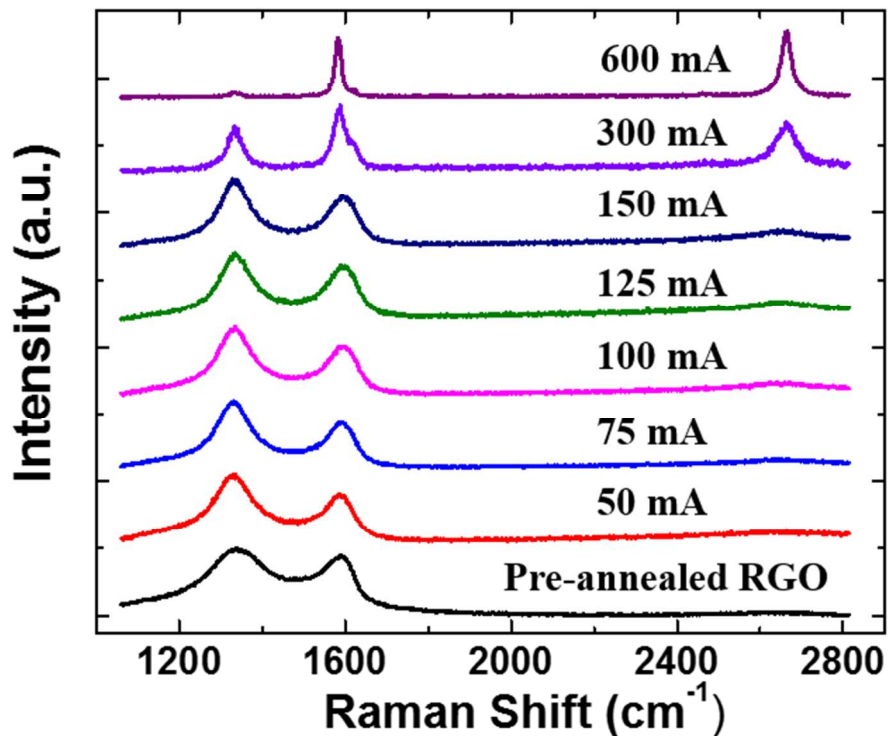
Joule heating process

The joule heating process was achieved by applying electrical current through freestanding RGO film in a vacuum chamber. The RGO film in the joule heating process is shown in Figure S1. The in situ temperature of the RGO film under joule heating was monitored by a spectrometer coupled with optical fiber, as shown in Figure 2a.

Figure S1. (a, b) Optical images of pre-annealed RGO film under current induced high temperature process. The high temperature process accompanied by a bright light, as shown in (b). Insert is the digital image taken by iphone6. (a) Scale bar represents 500μm. The optical morphology of RGO film after joule heating is shown in (c).

Raman characterizations of joule heated RGO film

Figure S2. Raman spectroscopy of RGO film sample (1800 μm long, 460 μm wide, and 1.25 μm thick) in the joule heating process. Overall, D peak at around 1350 cm^{-1} is suppressed and G peak at around 1600 cm^{-1} is encouraged as the current increases in the process which corresponding to the increased temperature. After current annealing at 600 mA, I_D/I_G decreased from 1.07 to 0.07 compared with primary 773K pre-annealed RGO. Meanwhile, the width of G peak narrows from 229 cm^{-1} to 76 cm^{-1}. 2D peak at around 2690 cm^{-1} shows up after 300 mA current annealing. All of above confirm that the RGO film have transformed into high quality graphene film with high crystallinity in the joule heating process.

# Morphology of joule heated RGO film
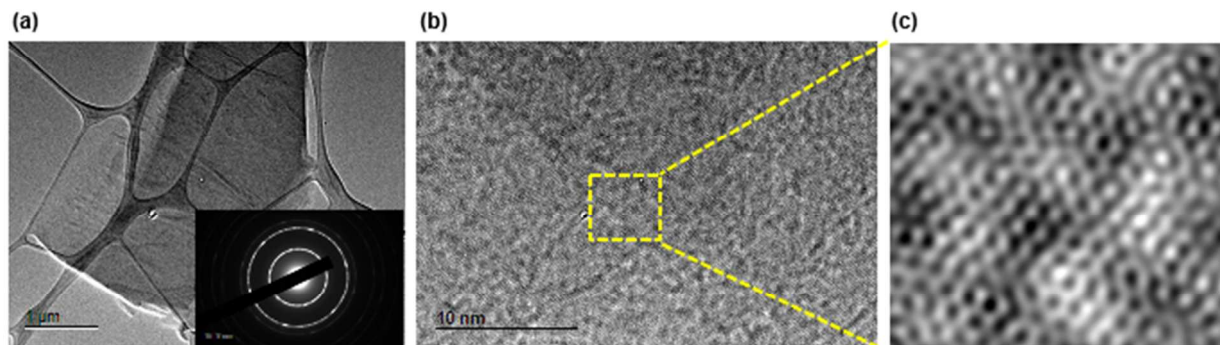
Figure S3. TEM images of the joule heated RGO at 2750K (a, b) with different magnifications, and filtered image (c). Insert of (a) is the corresponding selected area electron diffraction (SAED) pattern. This pattern shows the typical six-fold symmetry expected for graphene. Joule heated RGO film under 2750K shows high crystallinity with a few defects.
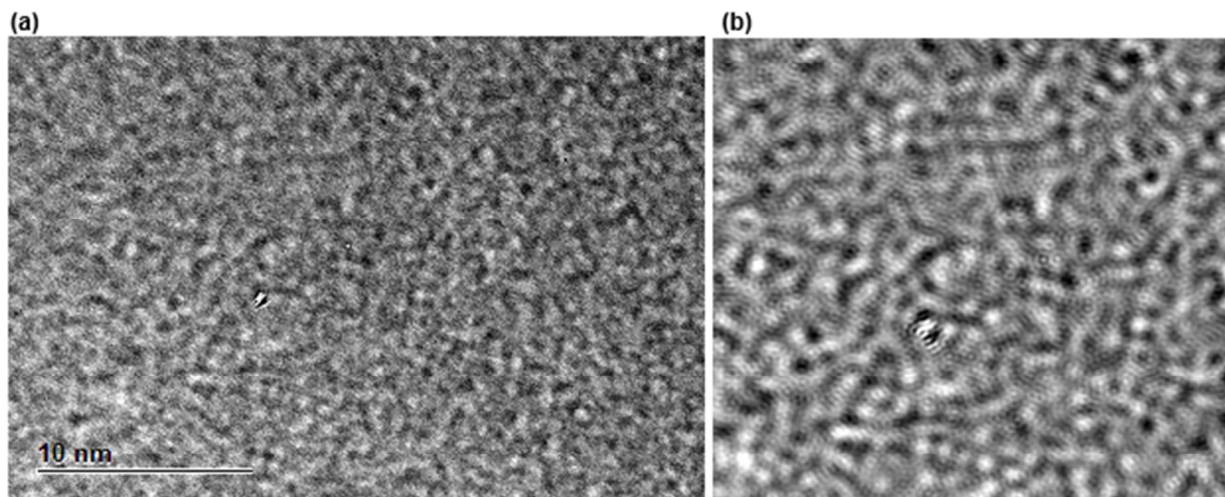
Figure S4. TEM image of joule heated RGO at 1700K (a) and filtered image (b). 1700K treated RGO film by joule heating shows the poor crystallinity.

Molecular dynamics simulations

C-C bonds in the graphene as well as the non-bonded C-C interactions are described by AIREBO potential.[2] The simulations are carried out using Large-scale Atomic/Molecular Massively Parallel Simulator (LAMMPS).[3] We design a bilayer graphene model with line slit defect with width about 0.48 nm and length about 0.77 nm. The slits have the equal spacing of about 2.58 nm. Periodical boundary condition are applied in all three dimensions. The graphene layers have periodical edges in along x and y direction. The interlayer distance (along z direction) is initially set as 1.36 nm. The simulation box has a dimension of 9.715 nm (x) by 9.798 nm (y) by 4 nm (z). Energy minimization simulations are first done by conjugate gradient (CG) algorithm followed by steepest descent algorithm until either the total energy change between successive iterations divided by the energy magnitude is less than or equal to 10^{-6} or the total force is less than 10^{-5} eV Å^{-1}. After energy minimization, the resulting structure is first heated up from 300 K to 2500 K in 400 ps, then maintained at 2500 K for another 400 ps. The time step for all simulations is set to be 0.001 picoseconds (ps), running in NVT ensemble and by Nose-Hoover thermostat.
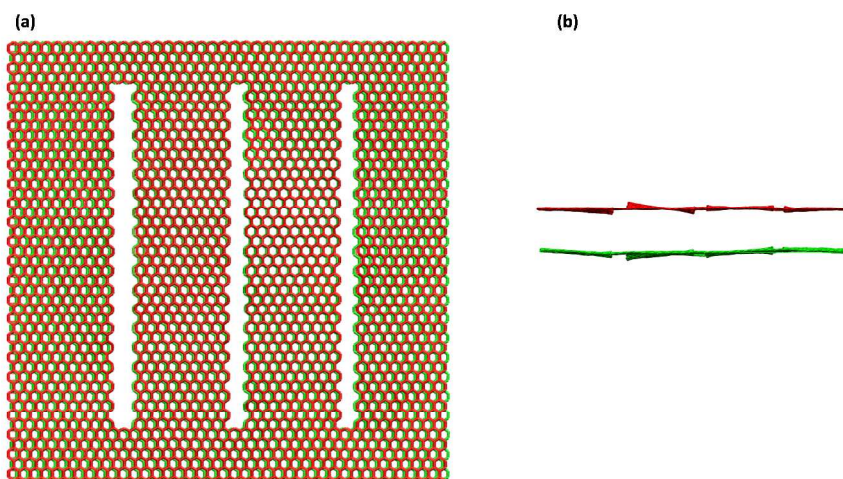
Figure S5. Simulation model description. (a) top view. (b) side view.

Figure S6a shows that at 1420K, our simulation model does not exhibit interlayer bonding. Figure S6b roughly denotes two observed interlayer bridging region at 1773 K. Region r1 shows that the left edge of a slit in top layer is fully bonded with the right edge of a slit in bottom layer. Region r2 shows only several bridging bonds form from near the end of the slit. At 2500 K, the left edges of all three slits in top layer are bonded with the right edges of all three slits in bottom layer, as denoted by Region R3 to R5 in Figure S6c.
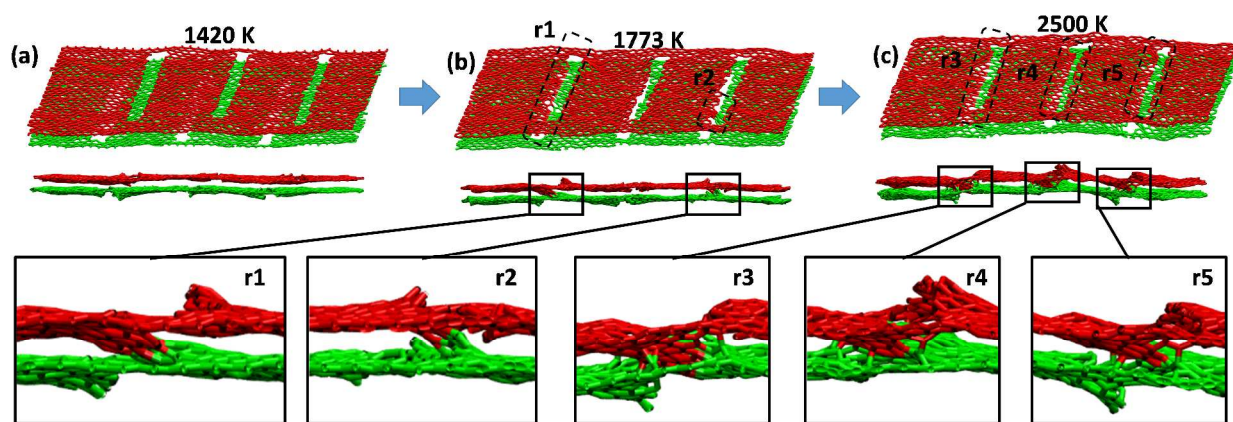
Figure S6. Molecular dynamics simulations results illustrating the formation of bonds between two defective graphene layers during temperature increase. Results at three representative temperatures are shown. Top row: perspective view. Middle row: side view. Bottom row: representative zoomed view at five bonding regions (r1 to r5). Note that region r2 is showing that bonds from starting near one end of the slit.

Calculation on the dimensions of the current collectors

A standard 18650 cell configuration was used to estimate the IR drop due to the resistance of current collectors. In 18650 cell configuration, the length is 600 mm, width is 50 mm (roughly) and I total is 0.6 A for a current density of 2 mA/cm^2. Tabs were used on the top of the RGO film current collector to conduct current and decrease the IR drop. The dependence of IR drop on the number of tabs and the film sheet resistance was calculated as below:

$$\Delta V = IR_s \frac{L}{WN^2}$$

Where R_s is the sheet resistance, N is number of tabs, L is length and W is width.

SEM image of the interface between RGO current collector and Li ion battery cathode
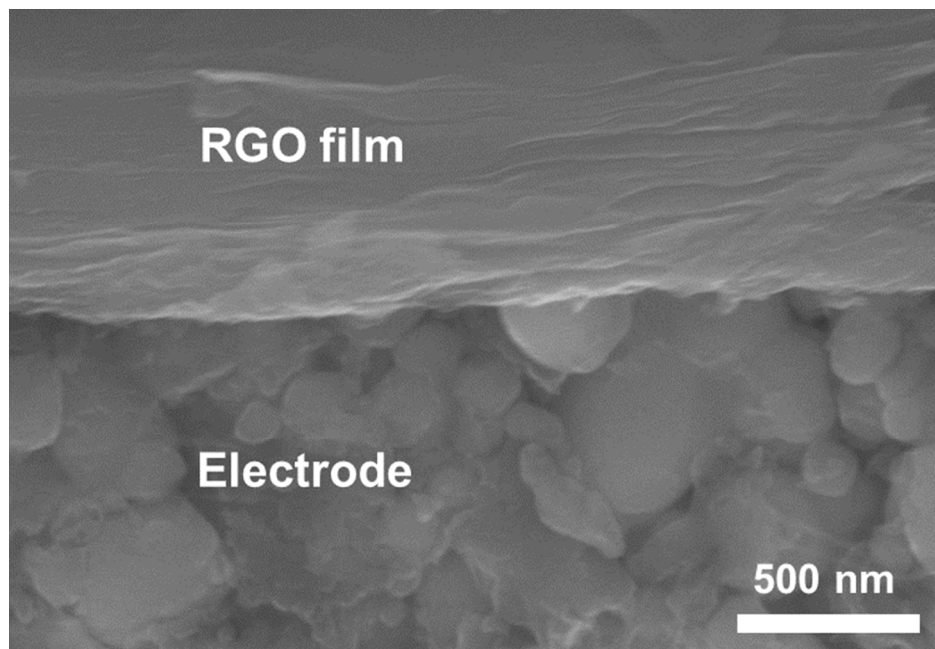
Figure S7. Magnified SEM image of the interface between electrode and RGO film current collector, indicating close contact at the electrode/RGO interface.

Electrochemical performance of electrode with Al current collector
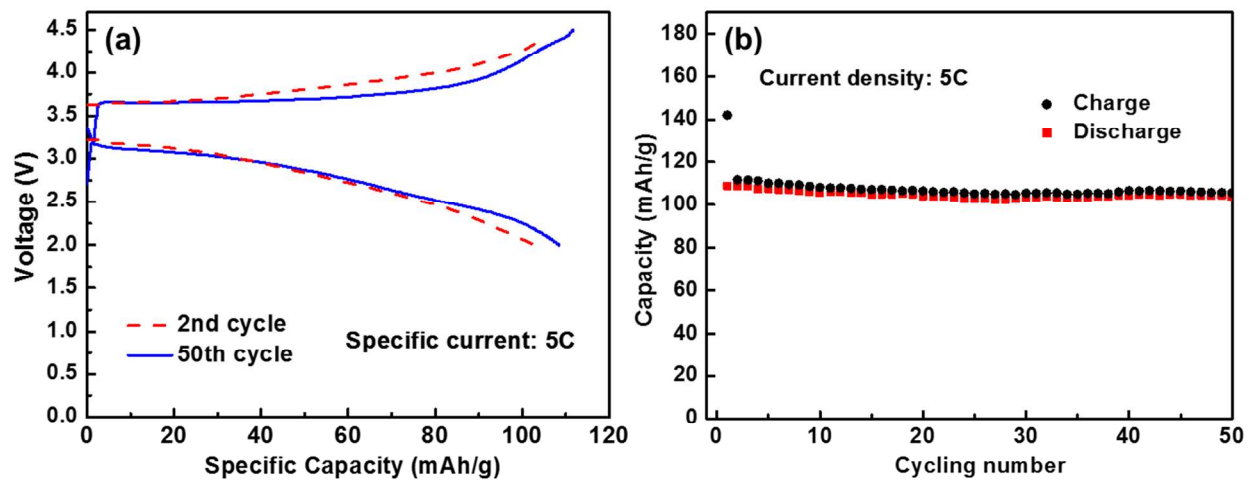
Figure S8. (a) Galvanostatic discharge/charge profiles of the LiFePO$_4$ electrode with Al current collector for the 2nd and 50th cycles. These tests were conducted in the potential range of 2–4.5 V vs. Li/Li$^+$ at 5C. (b) Cycling performance of the LiFePO$_4$ electrode with Al current collector at 5C.

Electrochemical stability of RGO film

To investigate the electrochemical stability of RGO film, a half cell was assembled and cyclic voltammetry (CV) measurement was conducted using RGO as the positive electrode and Li foil as the counter and reference electrode. The scan rate is 0.5 mV s^{-1}. As shown in Figure S9, during the voltage range of 2.0 V~4.0 V, there is no redox peak and the current density is negligible. It indicates that there is no side reaction and only the adsorption/desorption of ions occurs. At high voltage range of 4.0 V~4.5 V. There shows a flat and broad peak in the 1st cycle, which may be the decomposition of liquid electrolyte. These results indicate that the RGO current collector has good electrochemical stability.
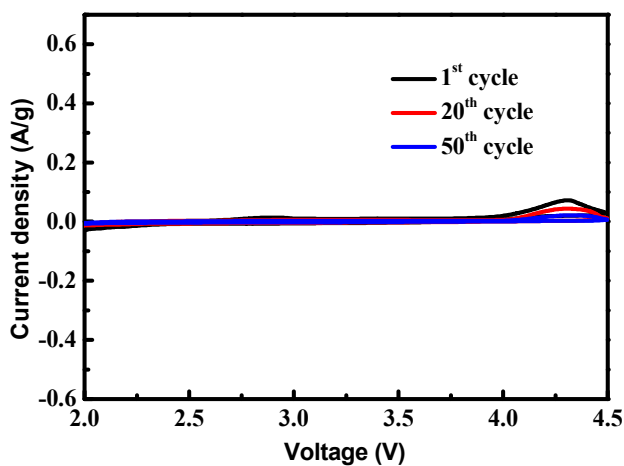

Figure S9. CV curves of the RGO film scanned at 0.5 mV s^{-1} in the potential range of 2–4.5 V vs. Li/Li^{+}.

Mechanical properties of RGO film

Mechanical tensile tests with the strain ramp rate of 0.2% min^{-1} were conducted on RGO samples which were thermally annealed at two different temperatures (2750 and 773 K). The results of these tests were compared to the tensile test of commercial Al foil current collector. The Al foil used for mechanical testing had a thickness of 16μm and an areal density of 4.28 mg/cm^2.

As shown in Figure S10, the tensile strengths of 2750K RGO film and 773K RGO film are 28.4 MPa and 17.1 MPa, respectively. From a thermal treatment at 2750K to a thermal treatment at 773K, there is a 66% increase in the tensile strength. However, numerous efforts still are needed to improve the tensile strength of 2750K RGO film in order to compete with the tensile strength of commercial Al foil, having a value of 188 MPa (Figure S11).
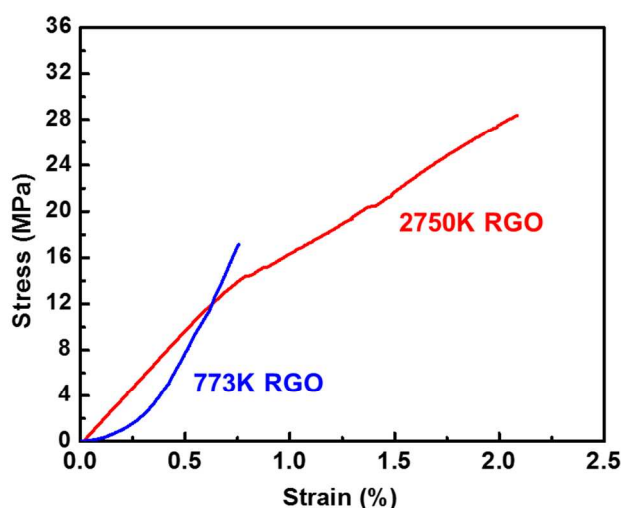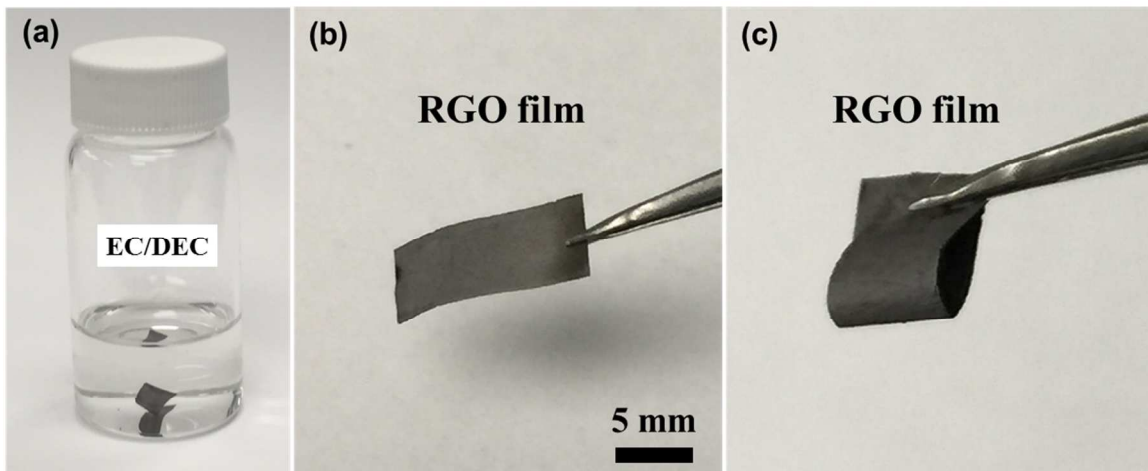

Figure S10. Stress–strain curve for 773K RGO and 2750K RGO. The tensile strength of 2750K RGO is 28.4 MPa compared with 17.1 MPa of 773K RGO.
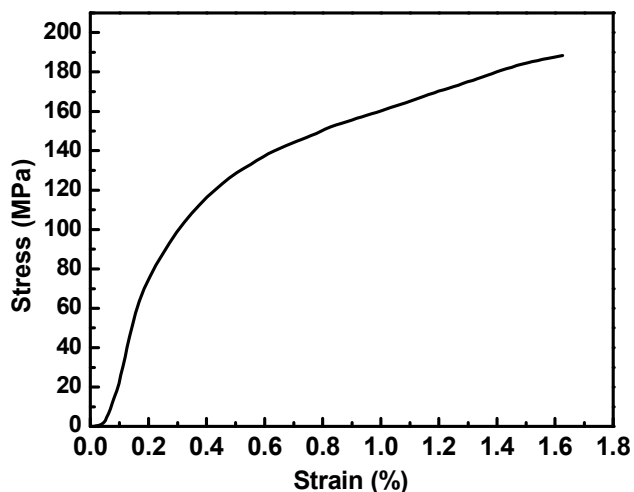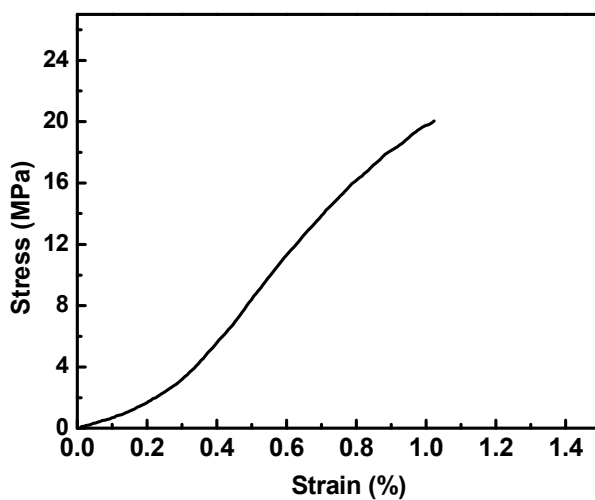
Figure S11. Stress–strain curve for commercial Al foil. The tensile strength of commercial Al foil is 188 MPa.

To investigate the mechanical stability of RGO film in liquid electrolyte, the 2750K RGO film (15mm long, 5mm wide and 4μm thick) was soaked in an ethylene carbonate/diethyl carbonate (EC:DEC = 1:1 by volume) solution for 3 days (Figure S12a) and then dried at 80℃ in vacuum oven for 24 hours. After being soaked, the RGO film still exhibited good mechanical stability. As shown in Figure S12b and Figure S12c, the soaked RGO film still can be bent almost 180° by tweezers, indicating its good flexibility. The tensile strength is 20.1 MPa for the RGO film after being soaked (Figure S13), which is slightly decreased from the 28.4 MPa seen in the as-annealed 2750K RGO film.

Figure S12. (a) Digital image showing RGO film soaking in NMP solution. (b) and (c) are images showing the flexibility of RGO film after being soaked and dried.


Figure S13. Stress–strain curve for 2750K RGO after immersing in liquid electrolyte (EC/DEC) for 3 days. The tensile strength is 20.1 MPa.

Stability of RGO film in slurry coating process

To investigate the structure stability of RGO film in slurry coating process, the 2750K RGO film was soaked in NMP solution for 3 days (Figure S14a) and then dried at 80℃ in vacuum oven for 24 hours to mimic the real operation of electrode slurry coating process. As shown in Figure S14b and Figure S14c, the RGO film maintained good flexibility and stable structure without swelling, demonstrating the compatibility of an RGO current collector with the commercial slurry coating process.
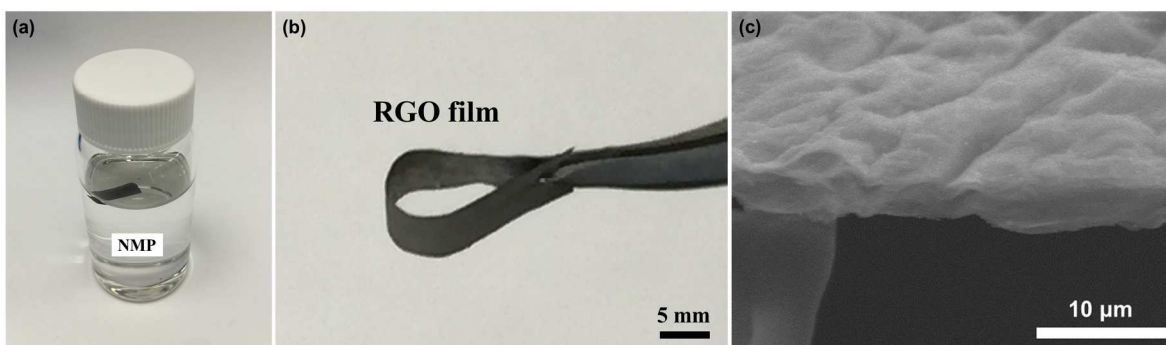
Figure S14. (a) Digital image showing RGO film being soaked in NMP solution. (b) Digital image exhibiting the flexibility of RGO film after soaked in NMP solution for 3 days. (c) SEM image showing the morphology of RGO film after being soaked.

Table. S1 Comparison of electrical properties of our RGO film and RGO or graphene based nanostructures (film, fiber) from previous reports.

Sample	preparation method	Electrical(S/cm) conductivity	ID/IG	Ref
RGO film	Current annealing	3112	0.019	This work
RGO film	Chemical reduction, Liquid-Mediated	33	1.38	39
RGO film	Hydrazine reduction	72	/	43
Graphene paper	Hydrazine reduction, 500 ℃ annealing	351	/	42
RGO fiber	Thermal annealed (2800 ℃)	416	0.01	18
Graphene film	Thermal annealed (1100 ℃)	727	1.4	38
RGO transparent conductive film	Hydroiodic acid reduction	1190	/	26
RGO-PDI	Thermal annealed (1000 ℃)	1314	/	41
RGO fiber	Thermal annealed (2850 ℃)	1790	0.001	40

Reference
(1) Marcano, D. C.; Kosynkin, D. V.; Berlin, J. M.; Sinitskii, A.; Sun, Z.; Slesarev, A.; Alemany, L. B.; Lu, W.; Tour, J. M. *ACS Nano.* **2010**, *4*, 4806–4814.
(2) Stuart, S. J.; Tutein, A. B.; Harrison, J. A. *J. Chem. Phys.* **2000**, *112*, 6472–6486.
(3) Plimpton, S. *J. Comput. Phys.* **1995**, *117*, 1–19.